ACSNANO

www.acsnano.org

ARTICLE

Domain Wall Automotion in Three-Dimensional Magnetic Helical Interconnectors

Luka Skoric,* Claire Donnelly, Aurelio Hierro-Rodriguez, Miguel A. Cascales Sandoval, Sandra Ruiz-Gómez, Michael Foerster, Miguel A. Niño, Rachid Belkhou, Claas Abert, Dieter Suess, and Amalio Fernández-Pacheco*

Cite This: *ACS Nano* 2022, 16, 8860–8868

Read Online

ACCESS | Metrics & More | Article Recommendations | Supporting Information

ABSTRACT: **The fundamental limits currently faced by traditional computing devices necessitate the exploration of ways to store, compute, and transmit information going beyond the current CMOS-based technologies. Here, we propose a three-dimensional (3D) magnetic interconnector that exploits geometry-driven automotion of domain walls (DWs), for the transfer of magnetic information between functional magnetic planes. By combining state-of-the-art 3D nanoprinting and standard physical vapor deposition, we prototype 3D helical DW conduits. We observe the automotion of DWs by imaging their magnetic state under different field sequences using X-ray microscopy, observing a robust unidirectional motion of DWs from the bottom to the top of the spirals. From experiments and micromagnetic simulations, we determine that the large thickness gradients present in the structure are the main mechanism for 3D DW automotion. We obtain direct evidence of how this tailorable magnetic energy gradient is imprinted in the devices, and how it competes with pinning effects that are due to local changes in the energy landscape. Our work also predicts how this effect could lead to high DW velocities, reaching the Walker limit during automotion. This work demonstrates a possible mechanism for efficient transfer of magnetic information in three dimensions.**

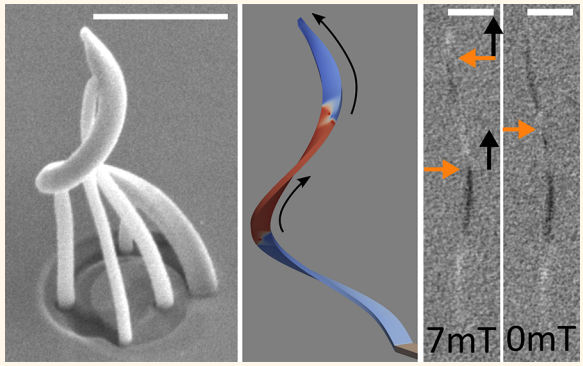

KEYWORDS: *spintronics, 3D nanofabrication, X-ray microscopy, domain walls, automotion*

The exponentially increasing demands of the information age for denser, more-efficient, and better-connected computing devices pose significant challenges to the microelectronics industry. Instead of relying purely on horizontal scaling, one way to address this is to start vertically stacking computing elements, a concept incorporated in the modern 3D V-NAND memories.[1] In addition to offering higher densities, the move to 3D would offer a route toward higher integration and improved connectivity, enabling computing paradigms going beyond von Neumann architectures, such as neuromorphic computing.[2]

An area that would particularly benefit from the advance to 3D technologies is spintronics. While offering robust, low-power, and nonvolatile devices,[3] current 2D spintronic technologies are lacking in densities when compared to their CMOS counterparts.[4] On the other hand, the low power consumption of spintronic devices makes them particularly well-suited to vertically integrated technologies where heat removal starts becoming problematic.[5] Going to 3D would allow us to leverage the many unique effects that arise in 3D nanomagnetic structures that could offer further scaling and increased functionality of computing elements.[6−8] In order to achieve this, however, it is necessary to develop 3D interconnectivity in magnetic devices without requiring multiple energetically costly charge-to-spin conversion steps. It is thus important to find efficient mechanisms to transfer magnetic information between planes using entirely magnetic interconnectors.

First steps toward highly interconnected spintronics[9] have been made by demonstrating the propagation of pure spin currents in 3D nanochannels[10] and high level of control over the domain walls (DWs) in 3D nanomagnetic conduits using external magnetic fields.[11] In addition to external stimuli, DWs can also be efficiently moved under the influence of geometry,

Received: November 21, 2021
Accepted: May 6, 2022
Published: May 17, 2022

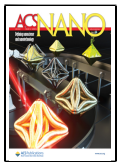

driven by intrinsic spin-structure changes. This so-called DW automotion has been previously studied in 2D[12−14] and is a promising mechanism that could allow fast, low-power, and robust transfer of magnetic information. In particular, using geometry-induced motion, the information could be transferred between functional planes where the state-of-the-art spintronic tools can be applied (Figure 1a).

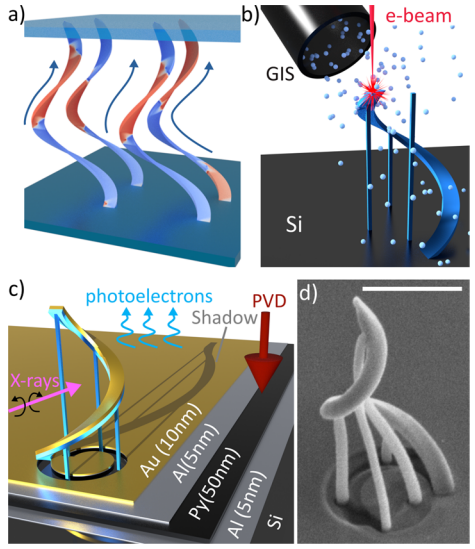

Figure 1. Fabrication of 3D magnetic interconnectors. (a) Concept device using 3D interconnectors to transfer magnetic information between two functional planes. (b) Scaffold for the DW conduit fabricated with FEBID using MeCpPt(Me)$_3$ precursor on a Si substrate. The scaffold is a 3 μm inward-curving spiral with four supporting pillars for mechanical stability. (c) Functional films deposited using physical vapor deposition (PVD) onto the structure and the substrate. Because of the directionality of PVD, the supporting pillars and the area directly beneath the structure are free from PVD materials. The magnetic state of the structure is investigated with the shadow X-ray magnetic circular dichroism photoemission electron microscopy (shadow XMCD-PEEM) method by comparing the signal from right-handed circularly polarized X-rays and left-handed circularly polarized X-rays. (d) SEM image taken at 45° tilt of the resulting structure after X-ray irradiation is shown. A mild initial bending of the original FEBID scaffold when exposed to PEEM environment is observed, after which the structure becomes stable (see section S1 in the Supporting Information for details). Scale bar = 1 μm.

While there are several ways in which the geometry of a system can be exploited to induce DW automotion, here we focus on three main effects: curvature gradients,[15,16] changes in the cross-section of magnetic material,[14,17] and magnetostatic interactions with magnetic surface charges. Specifically, we design a prototype 3D magnetic nanostructure in order to investigate the viability of the geometry-driven DW motion using state-of-the-art 3D nanofabrication.

We realize our prototype 3D automotive devices by harnessing focused-electron-beam-induced deposition (FEBID) to deposit a smooth, 3-μm-tall, 150-nm-wide, spiral scaffold with nonmagnetic C−Pt material (Figure 1b).[18] The spiral geometry is also particularly appealing because of its potential to vertically interconnect multiple planes with a small form factor, and for the underlying physics associated with its chiral geometry.[19,20] The spiral has an increasing out-of-plane tilt and smoothly curves inward. Following a previously developed fabrication procedure,[11,21] we subsequently deposit functional materials with physical vapor deposition (PVD) via thermal evaporation perpendicular to the substrate onto the entire sample (Figure 1c). For the magnetic layer, we use 50 nm of permalloy ($Ni_{80}Fe_{20}$), because of its low coercive fields, and good DW conduit properties.[22,23] We sandwich the permalloy layer with 5-nm Al layers to prevent oxidation, and add a 10-nm Au capping layer that serves as a highly efficient source of photoelectrons in shadow-PEEM and suppresses the XMCD signal from the Py on the substrate.[24]

The fabricated conduit combines magnetostatic interactions, curvature, and thickness gradients, all three of which are mechanisms for DW automotion, as discussed earlier. First, curvature is known to induce an effective Dzyaloshinskii−Moriya interaction (DMI) and anisotropy[19,25−27] that can lead to the DW automotion or pinning in curvilinear systems with inhomogeneous curvature.[15,16] In our structure, this is implemented by the inward curving spiral geometry, with a curvature gradient of 0.09 μm^{-2} in its central region (see section S2 in the Supporting Information). While the 3D wires also contain torsion, it is expected to introduce negligible quadratic corrections to the automotion, unless the motion is also driven by spin torques.[15,28] Second, changes in the cross-sectional area are known to strongly affect the DW energy landscape, preferentially moving it toward smaller cross sections,[17] which is an effect that has been experimentally demonstrated in 2D ferromagnetic rings.[14] Taking advantage of the directionality of evaporation, by the increasing steepness of the structure, we induce a negative thickness gradient, and thus a decreasing cross-sectional area normal to the spiral surface with height. Based on the model of the fabricated spiral, an average thickness gradient of −5.3 nm/μm is obtained in this way (see section S2 in the Supporting Information). In 2D films, thickness gradients are often achieved using moving shutters[29,30] or plasma-enhanced chemical vapor deposition methods,[31] which create wedge thin films on a scale of tens of micrometers to millimeters. Thus, the highly spatially varying thickness gradients achieved with 3D nanopatterning present a powerful advantage of this 3D fabrication procedure.

Finally, while the bottom of the spiral is connected to the substrate film, the top is freely standing, which results in the formation of magnetic surface charges. These can interact with the DW charges, inducing its motion. The strength of the magnetostatic interaction reduces rapidly with the distance from the edge. Therefore, these interactions are negligible in extended systems such as complex circuits where DWs are far from the edges. However, they are important to consider when investigating finite systems such as the ones in this work.

RESULTS AND DISCUSSION

Micromagnetic Simulations. To investigate the effect of the geometry on the DW automotion and determine the dominant automotive force in our system, we first perform dynamic finite-element micromagnetic simulations (see the Methods section). We use the model of the 3D structure closely matching the investigated spiral (see section S2 in the Supporting Information). Starting from the magnetization in a head-to-head configuration (Figure 2a, part (i), we observe the formation of a vortex DW (Figure 2a, part (ii), which moves up purely under the influence of the geometry (Figure 2a, part (iii), and ultimately fully switches the structure (Figure 2a, part (iv). As the DW moves through the structure (blue line in

https://doi.org/10.1021/acsnano.1c10345
ACS Nano 2022, 16, 8860−8868

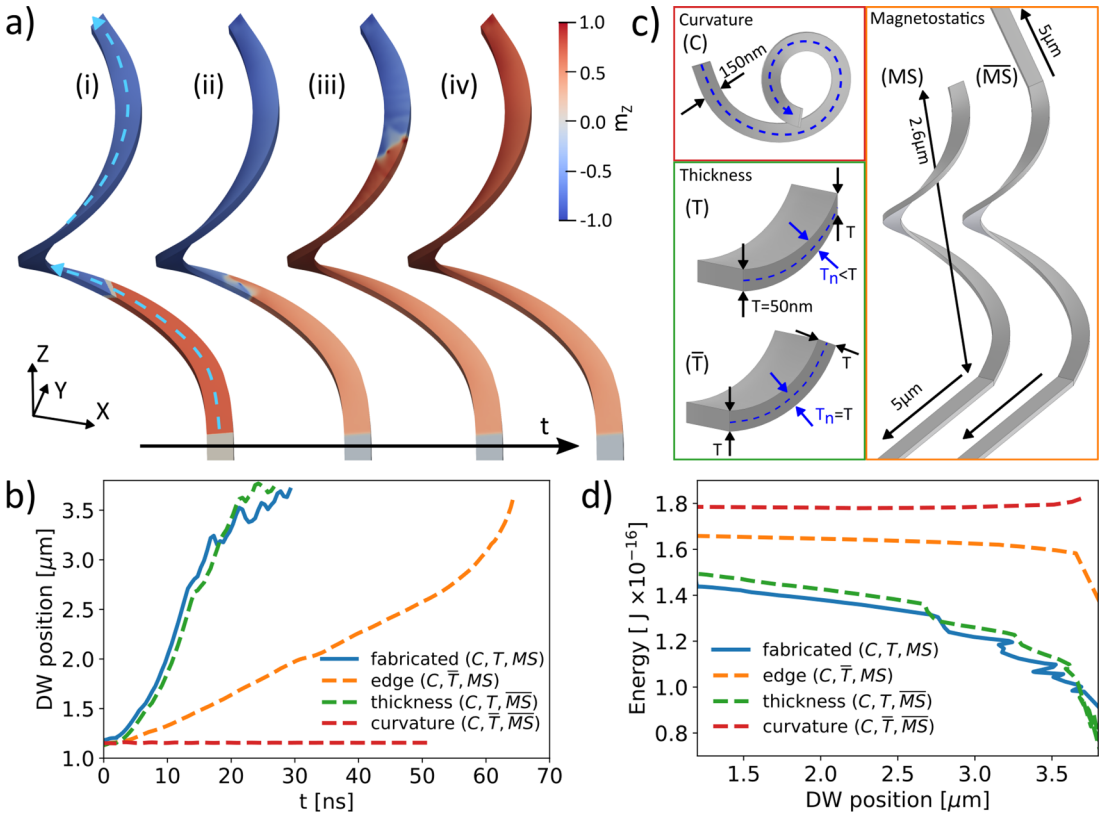

Figure 2. Simulations of DW automotion in 3D conduits. (a) Simulation snapshots for a model matching the fabricated structure: (i) initialization, (ii) relaxation into a DW, (iii) DW motion, (iv) final state. The blue dashed line on (i) shows the spiral central line along which the DW position is measured. (b) Position of the DW during simulations, as a function of simulation time (the as-fabricated structure is shown in blue). (c) The relevance of different automotion effects is investigated by considering a spiral with curvature gradients (C), with (T) and without ($\overline{T}$) gradients in thickness, and with (MS) and without ($\overline{MS}$) surface charges at the top edge. The T case corresponds to a constant vertical thickness (T = 50 nm), whereas $\overline{T}$ corresponds to a constant normal thickness (T_n = 50 nm); the effect of the charges (MS) is removed by adding a 5-μm extension. All structures have a 5-μm extension at the bottom edge to simulate the continuous connection with the substrate. The curvature gradient (red line in panel (b)) is not enough to drive the DW motion by itself. While the edge magnetostatics (orange line in panel (b)) can drive the motion, the strongest effect is achieved by thickness gradients (green line in panel (b)). After 10 ns, speeds of 200 m/s are surpassed, with the DW exhibiting Walker breakdown and the characteristic oscillatory motion. (d) Energy evolution of the DW as a function of position on the spiral during motion. The edge magnetostatics (orange) driven motion shows a slow, steady decrease in energy that becomes steeper as DW approaches the top. The thickness-gradient-driven motion has, throughout, a more steeply decreasing energy with steplike drops in the Walker regime. For the case with "only curvature" (red), where no automotion is observed, the DW is initialized at different positions on the spiral and its energy measured upon relaxation.

Figure 2b), it accelerates toward the top, reaching speeds above 200 m/s (see sections S3 and S4 in the Supporting Information) before exhibiting the Walker breakdown. The characteristic Walker breakdown-induced oscillations[32] can be seen by the back-and-forth motion of the DW after t = 15 ns (see section S5 in the Supporting Information for details).

With such high velocities observed in the combined system, we consequently perform simulations on a modified model to determine the relative strengths of the driving mechanisms. First, we focus only on the curvature gradient-driven automotion. We suppress the effect of thickness present in the real structure by modifying the film cross-section to obtain uniform thickness (thickness panel in Figure 2c). Moreover, we suppress any significant magnetostatic interactions with the edge by adding a 5-μm extension (magnetostatics panel in Figure 2c). In the modified structure, the DW remains at the position where it was initialized, exhibiting no significant automotion (red line in Figure 2b). The weak effect of inhomogeneity of curvature is further reinforced by observing no significant changes in the energy of the system with DW initialized at different heights along the structure (red line in Figure 2d). This agrees with previous theoretical studies where an order of magnitude larger curvature gradients were used to induce automotion.[15]

We next introduce realistic edge magnetostatics by removing the top extension while keeping the model otherwise identical (magnetostatics panel in Figure 2c). This results in the DW moving steadily to the top, speeding up as it approaches the top of the structure (orange line in Figure 2b). However, the motion is slow (~30 m/s, see section S4 in the Supporting Information), compared to the original structure, with only a weak gradient in energy as the DW moves up (orange line in Figure 2d).

Finally, we remove the edge magnetostatics by again adding the 5-μm extension, and consider the influence of gradients in film thickness (thickness panel in Figure 2c). In the simulated structure with thickness gradient (green line in Figure 2b), the DW accelerates to the top with motion closely matching the as-fabricated structure that combines all three automotive effects. Because of the lack of additional magnetostatic effects, the motion is slightly slower, and the Walker breakdown delayed. Furthermore, the energy evolution of the purely

https://doi.org/10.1021/acsnano.1c10345
ACS Nano 2022, 16, 8860−8868

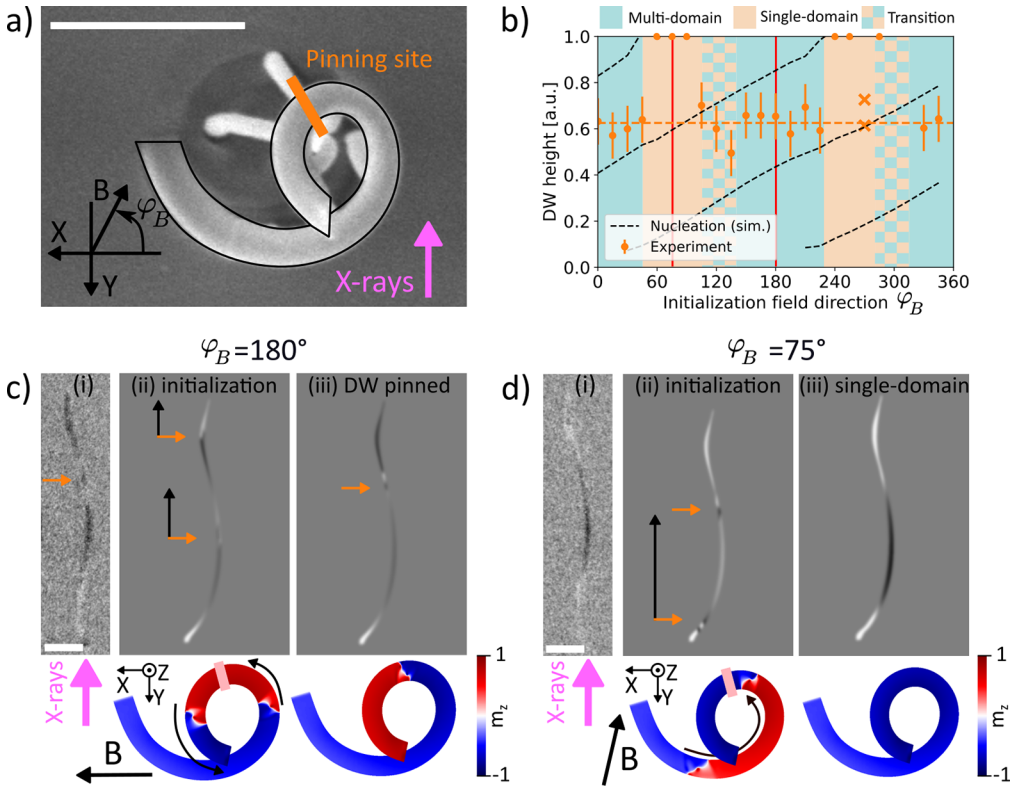

Figure 3. Angular study. (a) Top view of the fabricated structure (outline is present to guide the eye). The definition of the coordinate system is shown in bottom left, and the direction of X-rays denoted in pink. The location of the potential pinning site is shown in light pink. (b) Plot of the DW height normalized by the total structure height as a function of the initialization field angle φ_B (see section S10 in the Supporting Information for measurement details). Orange symbols correspond to experimental data, after removal of the initializing field and the following automotion. The black dashed lines represent the nucleation site (before automotion) of DWs as predicted by simulations. In the blue-shaded region, we measure multidomain final states with the DW position largely independent of the initialization angle (see panel (d), for example), suggesting a pinning site ~63% up the structure (orange dashed line). In the almond-shaded region, we experimentally observe single-domain final states denoted by the points at the top of the plot (see panel (c), for example). The checkerboard region indicates the transition region where both types of behaviors can be observed. At the points denoted by crosses, we observe states with DWs that are not fully annihilated (see section S12). The two vertical red lines denote the initialization directions shown in more detail in panels (c) and (d). (c) Initialization at 180°. Experiment (i) shows the DW in the upper part of the structure (orange arrow). X-rays are coming from below (pink arrow). Simulations (ii) and (iii) show the top view of the simulated initial structure state (Simulation (ii)) and the state closely matching the experiment (Simulation (iii)) colored by m_z (bottom), and the corresponding PEEM shadow (top). After the initialization (Simulation (ii)), both DWs (orange arrows) move up the structure (black arrows), with the snapshot matching the experimental state being the one with the single DW in the proximity to the pinning site (Simulation (iii)). (d) Initialization at 60° leads to single-domain state (Simulation (i)). Here, both DWs (orange arrows) are initialized below the pinning site (Simulation (ii)), and annihilated to reach the single-domain state (Simulation (iii)). All scale bars = 1 μm.

thickness-driven motion (green line in Figure 2d) approximately matches the fabricated structure (blue line in Figure 2d), with the Walker breakdown accompanied by the release of spin waves, resulting in the steplike decreases in energy. From this study, by combining different simulations, we conclude that the DWs in our structures are predominantly driven by the spatial modulation of film thickness, while the curvature gradients and the edge magnetostatics are secondary effects. Note that such a local gradient in thickness is difficult to realize in 2D devices.

Shadow-XPEEM Measurements. Having determined the dominant mechanism for DW automotion in the 3D interconnectors under investigation, we next use shadow X-ray magnetic circular dichroism photoemission electron microscopy (shadow-XPEEM) to experimentally investigate the automotion predicted by simulations. In shadow-XPEEM, the photoelectrons excited by the X-rays are measured in the shadow of the structure, exploiting X-ray magnetic circular dichroism (XMCD) to probe the magnetization parallel to the incident beam.[24,33] Since our structure has a complex 3D shape, interpreting the contrast is not trivial. Therefore, we supplement the experimental results by computing the resulting XMCD images of the micromagnetic simulations (see the Methods section).

In order to observe DW automotion experimentally, we measure the magnetic states of the spirals and the location of DWs as a response to magnetic fields. Specifically, we perform two types of experiments. First, in an "angular study", we test the entire device functionality by generating DWs at different positions within the structure. For this, we apply an in-plane saturating magnetic fields at different angles and measure the remanent state for each angle. Second, after understanding the behavior at multiple angles, we select a suitable angle for an "initialize and release" experiment, where we initialize a pair of DWs at a chosen angle (150°), and track their position as the magnetic field is reduced.

Angular Study. In the "angular study" we initialize the system with an in-plane saturating (70 mT) field in 15°

https://doi.org/10.1021/acsnano.1c10345
ACS Nano 2022, 16, 8860−8868

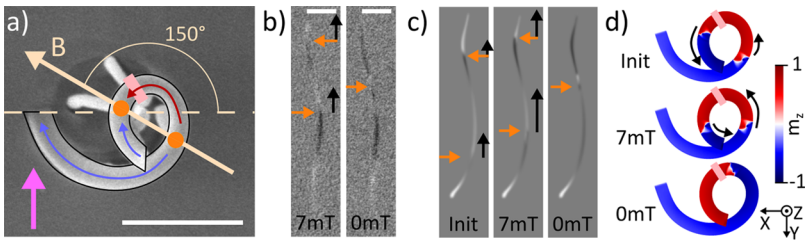

Figure 4. Depiction of the initialize and release methodology. (a) Top-view SEM image of the structure with outline to guide the eye. The direction of the applied field *B* is shown in yellow, and the direction of X-rays in pink. The schematic of the expected magnetization state at high field values before automotion, with the location of domains (blue and red arrows), DWs (orange dots) and the pinning site (light pink) are overlaid onto the structure. (b) Shadow-XPEEM snapshots of the magnetization states at 7 and 0 mT. All scale bars are 1 μm. (c) Simulated shadows for (0) as-initialized DW, (1) relaxed state for a 7mT field applied at 150° (corresponding to image 1 in panel (b)), (3) single DW simulation snapshot with the closest match to 0 mT (2) state in panel (b). Orange arrows in panels (b) and (c) indicate the positions of the DWs at each field value; black arrows indicate the upward automotion of the DWs observed between this and the following field value. (d) Top view of the simulation states colored by m_z corresponding to the computed PEEM contrast in panel (c).

increments, imaging the magnetic state of the spirals at remanence with a fixed X-ray direction (see Figure 3a for the definition of the coordinate system). Because of the spiral geometry, the DWs are initialized at positions where the spiral is perpendicular to the applied field. Depending on the field initialization angle, we observe two main regimes (Figure 3b): single-domain between 45° and 105° (and by symmetry between 225° and 285°), and multidomain between 315° and 45° (and by symmetry between 135° and 225°), with a narrow variable transition region between them. The multidomain regime contains a single DW, which is located at approximately the same place, between 50% and 70% up the structure height for the entire range of angles (orange dots in Figure 3b). For each of the regimes, we show the PEEM images along one example angle: 180° for multidomain (Figure 3c), and 75° for single-domain (Figure 3d). This behavior was found to be reproducible across an array of three structures, with the full data in section S12 in the Supporting Information.

To understand these experimental findings, we use simulations considering the state initialized by the applied magnetic field and the time evolution of the magnetization when the field is removed. Specifically, when the magnetic field is applied, two diametrically opposed DWs are formed (dashed lines in Figure 3b) that, in all cases, show a smooth upward automotion when the field is removed, ultimately leading to a single-domain state.

Therefore, the experiments showing multidomain states reveal the presence of pinning sites due to imperfections in the structures that compete against DW automotion. As the DWs initialized at different positions in the multidomain regime are consistently measured at the same place following relaxation, this implies that some have moved under no fields and have been pinned during automotion. Indeed, this final state is consistent with the systematic DW automotion up the structure after the field is removed, with a pinning site located ~63% up the structure. This location corresponds to the connection to one of the supporting legs (see Figure 3b), implying that the presence of this support introduced local changes in the magnetic energy landscape, most likely due to the changes in the strain of the film at that location.

The experimental finding that some angles lead to multidomain and others to single domain states can be understood by the location of the pinning site, relative to the two initialized DWs. For angles corresponding to the multidomain regime, the two initialized DWs are on opposite sides of this pinning site (see how the orange dashed line in Figure 3b is positioned between the two black dashed lines). The DW initialized above the pinning site is expected to escape through the top, while the one below gets stuck below the barrier. The same interpretation is also consistent with the single-domain regime. There, both DWs are initialized below the pinning site (see how both dashed lines in Figure 3b are positioned below the orange line). As they move up, they are forced into each other by automotion, annihilating at the barrier (see simulations in Figure 3d). In particular, the upper DW gets trapped in the pinning site first, leading to the interaction of both walls when the second also reaches this area. In most cases, both walls annihilate, leading to a single domain state as observed in the experiments (Figure 3d). However, in a few cases, we observe how the two domain walls are still present at remanence, being located around the pinning site region (see crosses in Figure 3b). The absence of annihilation is expected when the pinning of the lower wall is greater than its automotive effect, and also due to the possible presence of topological repulsion.[14,34] Furthermore, variations of DW structure for speeds above the Walker breakdown, and the stochastic nature of DW pinning processes will also result in a transition region between single-domain and multidomain states that is not sharp, with variances across the three measured structures (see section S12).

Initialize and Release Experiment. Following the angular study that allowed us to indirectly observe the effect of DW automotion and understand how DWs behave as a function of the direction of the initialization field, we next design an "initialize and release" experiment to directly track the automotion of the two DWs. For this, we initialize the structure with 70 mT fields at 150° (corresponding to the multidomain regime; see Figure 4a), and image the magnetic configuration of the spiral as the field is reduced to zero in discrete steps, measuring at 7, 4, and 0 mT (see Figure 4b for the cases corresponding to the two extreme values). Complementary simulations following the same protocol are also performed (see Figures 4c and 4d).

At 7 mT, we observe a multidomain state with the two DWs located below and above the pinning site, as in the initialization experiment discussed before (Figure 4b). Both domain walls are observed above the positions where they were initialized according to simulations (see Figures 4c and 4d), indicating that the reduction of the field from 70 mT to 7 mT has already allowed the automotion of DWs up the spiral. Indeed, when relaxing this simulated state under the application of 7 mT

https://doi.org/10.1021/acsnano.1c10345
ACS Nano 2022, 16, 8860−8868

field, both DWs move up and against the field, in agreement with the experimentally observed state.

Reducing further the field from 7 mT to 4 mT does not introduce a noticeable change in the experimental state (not shown here), implying that the automotion effect is smaller than the combined effect of pinning and the opposing external magnetic field. Removing the fields completely, in both the experiment and simulations, leads to the DWs moving up the spiral. We observe the upper DW escaping through the top, with the bottom one remaining pinned during automotion at ∼55% up the spiral, in good agreement with the position of the pinning site identified in the angular study. The direct observation of systematic upward motion of the DWs further confirms that DWs in this type of 3D magnetic interconnectors experience an automotive force that is purely geometrical in character, resulting in a spontaneous unidirectional motion into the third dimension, and representing a route toward low-energy magnetic interconnects.

CONCLUSIONS

In summary, in this work, we demonstrate the realization of 3D complex-shaped DW interconnectors that exhibit geometrically driven domain wall automotion. These devices are fabricated with a combination of FEBID 3D nanoprinting with high-quality magnetic materials deposited with PVD. Via micromagnetic simulations, we evaluate the strength of individual contributions to the automotion and identify the gradients in film thickness as the dominant contribution, capable of moving DWs at speeds above 200 m/s and inducing Walker breakdown. We demonstrate the validity of the concept using shadow-XPEEM by directly observing the reproducible automotion and investigating the pinning landscape in the fabricated devices. The realization of strong and spatially varying gradients in thickness, which are difficult to realize in 2D, represent an attractive prospect for domain wall manipulation in 3D architectures, and an interesting tool for functionalizing spintronic interconnectors. On the fundamental side, we envision this work to inspire further exploration of a variety of spin textures and their automotion in 3D.[15,35,36] The proposed concept could be exploited by scalable fabrication methods,[37] for a field- and current-free method for unidirectional magnetic information transfer between functional planes. This concept could help address two of the main challenges that spintronics faces when moving to three dimensions. First, although the motion of domain walls is well-controlled in 2D, robust motion in 3D interconnects has yet to be established. Second, current-driven domain wall motion in 3D suspended nanostructures without large heat sinks faces severe heat dissipation challenges. By providing a purely geometric transfer of information between planes—an "elevator effect"—DW automotive devices such as the one described here promise to circumvent these challenges and offer a route to the implementation of 3D spintronic devices, which have possible applications in high-density magnetic memories and unconventional computing.

METHODS

Fabrication. The 3D spiral scaffold was fabricated with MeCpPt(Me)$_3$ on *p*-doped Si substrate using focused-electron-beam-induced deposition with the Helios 600 system at the Wolfson Electron Microscopy Suite of University of Cambridge. The electron beam was set to 21 pA, 30 kV. Beam scanning patterns were created from the designed STL files, using the custom pattern generating software,[18] and the total fabrication time was 14 min per structure. Physical vapor deposition was done using an in-house thermal evaporator. The deposition rates were as follows: 3.75 nm/min for Al, 1.8 nm/min for $Ni_{80}Fe_{20}$, and 0.7 nm/min for Au. The structure imaged from multiple directions and further information on PEEM-induced deformation is available in section S1 in the Supporting Information.

Micromagnetic Simulations. All micromagnetic simulations were performed with the finite-element magnum.fe library.[38] We use the material parameters typical of permalloy: $M_S = 8 \times 10^5$ A m^{-1}, $A = 1.3 \times 10^{-11}$ J m^{-1}, and consider the exchange field, the demagnetization field, as well as the external field, but no magneto-crystalline anisotropy. The models were meshed with GMSH[39] with a characteristic mesh edge length of 5.7 nm. This corresponds to the permalloy dipolar exchange length l, which is defined as $l = \sqrt{\frac{2A}{\mu_0 M_S^2}} =$ 5.7 nm. The details of the simulation structure are available in section S2 in the Supporting Information.

In order to acquire the simulation results presented in Figure 2, a single DW is initialized 1 μm from the bottom in a head-to-head configuration with the magnetization tangential to the spiral. First, the state is relaxed into a DW by integrating the Landau−Lifshitz−Gilbert (LLG) equation with high damping (α = 1), simulating slow ramp-down of the fields after initialization. Second, the dynamics of the DW are investigated by again relaxing with LLG, now using realistic damping for permalloy (α = 0.01).

The simulations presented in the angles study (Figure 3b, initializations in Figures 3c and 3d, and in the section S12 in the Supporting Information were acquired by starting from the magnetization fully pointing in the direction of the corresponding magnetic field. The state is then integrated with LLG using high damping (α = 1) and stopping once the DW is formed. The simulation states showed in Figures 3c and 3d (Simulation (iii)) are snapshots where the shadow most closely matches the simulated state, since, because of the lack of pinning, simulated DWs always propagate to the top of the structure.

The simulations presented in Figure 4c are acquired by starting from the magnetization pointing in the 150° direction, with a small (10°) tilt introduced to prefer left-handed vortex DW circulation that better matches the data (see section S11 in the Supporting Information for details). As observed previously, the state is first relaxed into a DW with high damping (α = 1). The state is further integrated under 7 mT external fields with LLG using realistic damping (α = 0.01) to allow DW dynamics (Figure 4c, part 1). Finally, the effect of removal of the field is observed by removing the external field term, and further evolving the LLG (Figure 4c, part 2).

Shadow-XPEEM. Shadow-XPEEM images were taken at the CIRCE beamline of the ALBA Synchrotron Light Facility.[40] The X-ray beam incident at 16° was set to ∼1 eV below the Fe L_3 edge (see section S7 in the Supporting Information for XAS spectra). The start voltage was 6.0 V, and the contrast aperture was 30 μm. In situ fields were applied using an improved version of the sample holder with quadrupole in-plane electromagnet described in ref 41. which allows larger field values due to a reduced gap size in the magnetic yoke. For the details of image processing procedure, see section S8 in the Supporting Information and the corresponding software in ref 42. The simulated images were generated from micromagnetic simulations, using a custom ray tracing code described in ref 43 (see section S9 in the Supporting Information).

Measuring Domain Wall Position. In order to determine the variation of the DW position as a function of initial angle (Figure 3b), the position of the DW in the shadow is measured from the bottom of the structure, normalized by the total shadow length. The location of the DW wall is acquired by plotting the XMCD signal as a function of position in the shadow and looking for regions of rapidly changing contrast, signifying the presence of the DW. For details, see section S10 in the Supporting Information.

https://doi.org/10.1021/acsnano.1c10345
ACS Nano 2022, 16, 8860−8868

DATA AVAILABILITY

The raw experimental and computational data supporting the findings of this study are openly available at the DIGITAL.CSIC repository (http://hdl.handle.net/10261/268139).

CODE AVAILABILITY

The code used to produce XMCD images is available at 10.5281/zenodo.5094555,[42] and the code for simulations of XMCD images from micromagnetic simulations can be found at 10.5281/zenodo.5094531.[43]

ASSOCIATED CONTENT

Supporting Information

The Supporting Information is available free of charge at https://pubs.acs.org/doi/10.1021/acsnano.1c10345.

X-ray induced bending analysis; simulation structure details; method for calculating DW position; domain wall speed in simulations; Walker breakdown; effects of the mesh size; XAS spectra; shadow-XPEEM image processing; shadow-XPEEM simulation method; measuring DW height in simulations and experiments; domain wall chirality; full details of the angular study (PDF)

AUTHOR INFORMATION

Corresponding Authors

Luka Skoric − *Department of Physics, Cavendish Laboratory, University of Cambridge, Cambridge CB3 0HE, United Kingdom;* orcid.org/0000-0002-2169-3008; Email: ls604@cam.ac.uk

Amalio Fernández-Pacheco − *Insituto de Nanociencia y Materiales de Aragón (INMA), CSIC-Universidad de Zaragoza, 50009 Zaragoza, Spain;* orcid.org/0000-0002-3862-8472; Email: amaliofp@unizar.es

Authors

Claire Donnelly − *Department of Physics, Cavendish Laboratory, University of Cambridge, Cambridge CB3 0HE, United Kingdom; Max Planck Institute for Chemical Physics of Solids, 01187 Dresden, Germany;* orcid.org/0000-0002-9942-2419

Aurelio Hierro-Rodriguez − *SUPA, School of Physics and Astronomy, University of Glasgow, Glasgow G12 8QQ, United Kingdom; Depto. Física, Universidad de Oviedo, 33007 Oviedo, Spain*

Miguel A. Cascales Sandoval − *SUPA, School of Physics and Astronomy, University of Glasgow, Glasgow G12 8QQ, United Kingdom*

Sandra Ruiz-Gómez − *ALBA Synchrotron Light Facility, 08290 Cerdanyola del Vallès, Spain; Max Planck Institute for Chemical Physics of Solids, 01187 Dresden, Germany*

Michael Foerster − *ALBA Synchrotron Light Facility, 08290 Cerdanyola del Vallès, Spain*

Miguel A. Niño − *ALBA Synchrotron Light Facility, 08290 Cerdanyola del Vallès, Spain;* orcid.org/0000-0003-3692-147X

Rachid Belkhou − *SOLEIL Synchrotron, L'ormes des Merisiers, 91192 Gif-Sur-Yvette, Cedex, France*

Claas Abert − *Faculty of Physics, University of Vienna, 1010 Vienna, Austria; Research Platform MMM Mathematics-Magnetism-Materials, University of Vienna, 1010 Vienna, Austria*

Dieter Suess − *Faculty of Physics, University of Vienna, 1010 Vienna, Austria; Research Platform MMM Mathematics-Magnetism-Materials, University of Vienna, 1010 Vienna, Austria*

Complete contact information is available at: https://pubs.acs.org/10.1021/acsnano.1c10345

Notes

The preprint version of this work has previously been submitted to arXiv under the following reference: Skoric, L.; Donnelly, C.; Hierro-Rodriguez, A.; Cascales Sandoval, M.; Ruiz-Gómez, S.; Foerster, M.; Orti, M. A. N.; Belkhou, R.; Abert, C.; Suess, D.; Fernández-Pacheco, A. Domain Wall Automotion in Three-Dimensional Magnetic Helical Interconnectors. 2021, 14. arXiv:2110.04636v1 [cond-mat.mes-hall], https://arxiv.org/abs/2110.04636v1 (Oct. 9, 2021).
The authors declare no competing financial interest.

ACKNOWLEDGMENTS

The authors thank G. Divitini, and other staff of the Wolfson Electron Microscopy Suite for their technical support. We also appreciate discussions with D. D. Sheka, R. P. Cowburn, P. Fischer, and R. Streubel. AFP thanks the Universities of Cambridge and Glasgow, where part of this research was conducted. All data was measured at CIRCE (BL-24) beamline at ALBA synchrotron in collaboration with ALBA staff (Proposal No. 2020024091). Preliminary measurements were performed at the HERMES beamline at SOLEIL synchrotron in collaboration with SOLEIL staff (Proposal Nos. 20200879, 20190565, and 20170904). This work was supported by the EPSRC Cambridge NanoDTC EP/L015978/1, the Winton Program for the Physics of Sustainability, the project CALIPSOplus (under Grant Agreement No. 730872 from the EU Framework Programme for Research and Innovation HORIZON 2020), and by the European Community (under the Horizon 2020 Program, Contract No. 101001290, 3DNANOMAG). L.S. acknowledges support from St. Johns College of the University of Cambridge. C.D. was supported by the Leverhulme Trust (No. ECF-2018-016), the Isaac Newton Trust (No. 18-08), and the L'Oréal-UNESCO UK and Ireland Fellowship For Women In Science. A.H.-R. acknowledges support from Spanish AEI, under Project Reference No. PID2019-104604RB/AEI/10.13039/501100011033. The authors acknowledge the University of Vienna research platform MMM Mathematics−Magnetism−Materials, the FWF (Project No. I 4917), and Aragon Government through the Project Q-MAD.

REFERENCES

(1) Park, K.-T.; Nam, S.; Kim, D.; Kwak, P.; Lee, D.; Choi, Y.-H.; Choi, M.-H.; Kwak, D.-H.; Kim, D.-H.; Kim, M.-S.; Park, H.-W.; Shim, S.-W.; Kang, K.-M.; Park, S.-W.; Lee, K.; Yoon, H.-J.; Ko, K.; Shim, D.-K.; Ahn, Y.-L.; Ryu, J.; et al. Three-Dimensional 128 Gb MLC Vertical Nand Flash Memory With 24-WL Stacked Layers and 50 MB/s High-Speed Programming. *IEEE J. Solid-State Circuits* **2015**, *50*, 204−213.

(2) Marković, D.; Mizrahi, A.; Querlioz, D.; Grollier, J. Physics for Neuromorphic Computing. *Nat. Rev. Phys.* **2020**, *2*, 499−510.

(3) Ji, Y.; Goo, H. J.; Lim, J.; Lee, S. B.; Lee, S.; Uemura, T.; Park, J. C.; Han, S. I.; Shin, S. C.; Lee, J. H.; Song, Y. J.; Lee, K. M.; Shin, H. M.; Hwang, S. H.; Seo, B. Y.; Lee, Y. K.; Kim, J. C.; Koh, G. H.; Park, K. C.; Pae, S. et al. Reliability of 8Mbit Embedded-STT-MRAM in 28nm FDSOI Technology. *2019 IEEE International Reliability Physics Symposium*; IRPS, 2019; pp 1−3.

(4) Dieny, B.; Prejbeanu, I. L.; Garello, K.; Gambardella, P.; Freitas, P.; Lehndorff, R.; Raberg, W.; Ebels, U.; Demokritov, S. O.; Akerman, J.; Deac, A.; Pirro, P.; Adelmann, C.; Anane, A.; Chumak, A. V.; Hiroata, A.; Mangin, S.; Onbasli, M. C.; d Aquino, M.; Prenat, G. et al. *Opportunities and Challenges for Spintronics in the Microelectronic Industry*, 2019, 10584. arXiv:1908.10584v1 [physics.app-ph]. https://arxiv.org/abs/1908.10584 (Aug. 28, 2019).
(5) Han, J.-H.; West, R. E.; Torres-Castro, K.; Swami, N.; Khan, S.; Stan, M. Power and Thermal Modeling of In-3D-Memory Computing. Presented at the *2021 International Symposium on Devices, Circuits and Systems (ISDCS)*, 2021; pp 1−4.
(6) Fernández-Pacheco, A.; Streubel, R.; Fruchart, O.; Hertel, R.; Fischer, P.; Cowburn, R. P. Three-Dimensional Nanomagnetism. *Nat. Commun.* **2017**, *8*, 15756.
(7) Streubel, R.; Fischer, P.; Kronast, F.; Kravchuk, V. P.; Sheka, D. D.; Gaididei, Y.; Schmidt, O. G.; Makarov, D. Magnetism in Curved Geometries. *J. Phys. D: Appl. Phys.* **2016**, *49*, 363001.
(8) Parkin, S.; Yang, S.-H. Memory on the Racetrack. *Nat. Nano* **2015**, *10*, 195−198.
(9) Burks, E. C.; Gilbert, D. A.; Murray, P. D.; Flores, C.; Felter, T. E.; Charnvanichborikarn, S.; Kucheyev, S. O.; Colvin, J. D.; Yin, G.; Liu, K. 3D Nanomagnetism in Low Density Interconnected Nanowire Networks. *Nano Lett.* **2021**, *21*, 716−722.
(10) Das, K. S.; Makarov, D.; Gentile, P.; Cuoco, M.; van Wees, B. J.; Ortix, C.; Vera-Marun, I. J. Independent Geometrical Control of Spin and Charge Resistances in Curved Spintronics. *Nano Lett.* **2019**, *19*, 6839−6844.
(11) Sanz-Hernández, D.; Hamans, R. F.; Liao, J.-W.; Welbourne, A.; Lavrijsen, R.; Fernández-Pacheco, A. Fabrication, Detection, and Operation of a Three-Dimensional Nanomagnetic Conduit. *ACS Nano* **2017**, *11*, 11066−11073.
(12) Richter, K.; Krone, A.; Mawass, M.-A.; Krüger, B.; Weigand, M.; Stoll, H.; Schütz, G.; Kläui, M. Local Domain-Wall Velocity Engineering via Tailored Potential Landscapes in Ferromagnetic Rings. *Phys. Rev. Applied* **2016**, *5*, 024007.
(13) Nikonov, D. E.; Manipatruni, S.; Young, I. A. Automotion of Domain Walls for Spintronic Interconnects. *J. Appl. Phys.* **2014**, *115*, 213902.
(14) Mawass, M.-A.; Richter, K.; Bisig, A.; Reeve, R. M.; Krüger, B.; Weigand, M.; Stoll, H.; Krone, A.; Kronast, F.; Schütz, G.; Kläui, M. Switching by Domain-Wall Automotion in Asymmetric Ferromagnetic Rings. *Phys. Rev. Appl.* **2017**, *7*, 044009.
(15) Yershov, K. V.; Kravchuk, V. P.; Sheka, D. D.; Pylypovskyi, O. V.; Makarov, D.; Gaididei, Y. Geometry-Induced Motion of Magnetic Domain Walls in Curved Nanostripes. *Phys. Rev. B* **2018**, *98*, 060409.
(16) Yershov, K. V.; Kravchuk, V. P.; Sheka, D. D.; Gaididei, Y. Curvature-Induced Domain Wall Pinning. *Phys. Rev. B* **2015**, *92*, 104412.
(17) Fernandez-Roldan, J. A.; De Riz, A.; Trapp, B.; Thirion, C.; Vazquez, M.; Toussaint, J.-C.; Fruchart, O.; Gusakova, D. Modeling Magnetic-Field-Induced Domain Wall Propagation in Modulated-Diameter Cylindrical Nanowires. *Sci. Rep.* **2019**, *9*, 5130.
(18) Skoric, L.; Sanz-Hernández, D.; Meng, F.; Donnelly, C.; Merino-Aceituno, S.; Fernández-Pacheco, A. Layer-by-Layer Growth of Complex-Shaped Three-Dimensional Nanostructures with Focused Electron Beams. *Nano Lett.* **2020**, *20*, 184−191.
(19) Volkov, O. M.; Sheka, D. D.; Gaididei, Y.; Kravchuk, V. P.; Rößzler, U. K.; Fassbender, J.; Makarov, D. Mesoscale Dzyaloshinskii-Moriya Interaction: Geometrical Tailoring of the Magnetochirality. *Sci. Rep* **2018**, *8*, 866.
(20) Donnelly, C.; Hierro-Rodríguez, A.; Abert, C.; Witte, K.; Skoric, L.; Sanz-Hernández, D.; Finizio, S.; Meng, F.; McVitie, S.; Raabe, J.; Suess, D.; Cowburn, R.; Fernández-Pacheco, A. Complex Free-Space Magnetic Field Textures Induced by Three-Dimensional Magnetic Nanostructures. *Nat. Nanotechnol.* **2022**, *17*, 136−142.
(21) Sanz-Hernández, D.; Hamans, R. F.; Osterrieth, J.; Liao, J.-W.; Skoric, L.; Fowlkes, J. D.; Rack, P. D.; Lippert, A.; Lee, S. F.; Lavrijsen, R.; Fernández-Pacheco, A. Fabrication of Scaffold-Based 3D Magnetic Nanowires for Domain Wall Applications. *Nanomaterials* **2018**, *8*, 483.
(22) Allwood, D. A.; Xiong, G.; Faulkner, C. C.; Atkinson, D.; Petit, D.; Cowburn, R. P. Magnetic Domain-Wall Logic. *Science* **2005**, *309*, 1688−1692.
(23) Nahrwold, G.; Scholtyssek, J. M.; Motl-Ziegler, S.; Albrecht, O.; Merkt, U.; Meier, G. Structural, Magnetic, and Transport Properties of Permalloy for Spintronic Experiments. *J. Appl. Phys.* **2010**, *108*, 013907.
(24) Wartelle, A.; Pablo-Navarro, J.; Staňo, M.; Bochmann, S.; Pairis, S.; Rioult, M.; Thirion, C.; Belkhou, R.; de Teresa, J. M.; Magén, C.; Fruchart, O. Transmission XMCD-PEEM Imaging of an Engineered Vertical FEBID Cobalt Nanowire with a Domain Wall. *Nanotechnology* **2018**, *29*, 045704.
(25) Sheka, D. D.; Pylypovskyi, O. V.; Landeros, P.; Gaididei, Y.; Kákay, A.; Makarov, D. Nonlocal Chiral Symmetry Breaking in Curvilinear Magnetic Shells. *Commun. Phys.* **2020**, *3*, 1−7.
(26) Phatak, C.; Liu, Y.; Gulsoy, E. B.; Schmidt, D.; Franke-Schubert, E.; Petford-Long, A. Visualization of the Magnetic Structure of Sculpted Three-Dimensional Cobalt Nanospirals. *Nano Lett.* **2014**, *14*, 759−764.
(27) Pylypovskyi, O. V.; Kravchuk, V. P.; Sheka, D. D.; Makarov, D.; Schmidt, O. G.; Gaididei, Y. Coupling of Chiralities in Spin and Physical Spaces: The Möbius Ring as a Case Study. *Phys. Rev. Lett.* **2015**, *114*, 197204.
(28) Yershov, K. V.; Kravchuk, V. P.; Sheka, D. D.; Gaididei, Y. Curvature and Torsion Effects in Spin-Current Driven Domain Wall Motion. *Phys. Rev. B* **2016**, *93*, 094418.
(29) Petr, M.; Kylián, O.; Hanuš, J.; Kuzminova, A.; Vaidulych, M.; Khalakhan, I.; Choukourov, A.; Slavínská, D.; Biederman, H. Surfaces With Roughness Gradient and Invariant Surface Chemistry Produced by Means of Gas Aggregation Source and Magnetron Sputtering. *Plasma Process. Polym.* **2016**, *13*, 663−671.
(30) Vishwakarma, P.; Gupta, M.; Reddy, V. R.; Phase, D. M.; Gupta, A. Study of Interfaces in Hf/Fe System Using Magneto-Optical Kerr Effect and Soft X-Ray Absorption Spectroscopy. *Phys. Status Solidi RRL* **2020**, *14*, 2000177.
(31) López-Santos, M.-C.; Alvarez, R.; Palmero, A.; Borrás, A.; del Campo, R. C.; Holgado, M.; González-Elipe, A. R. Micron-Scale Wedge Thin Films Prepared by Plasma Enhanced Chemical Vapor Deposition. *Plasma Process. Polym.* **2017**, *14*, 1700043.
(32) Schryer, N. L.; Walker, L. R. The Motion of 180° Domain Walls in Uniform dc Magnetic Fields. *J. Appl. Phys.* **1974**, *45*, 5406−5421.
(33) Kimling, J.; Kronast, F.; Martens, S.; Böhnert, T.; Martens, M.; Herrero-Albillos, J.; Tati-Bismaths, L.; Merkt, U.; Nielsch, K.; Meier, G. Photoemission Electron Microscopy of Three-Dimensional Magnetization Configurations in Core-Shell Nanostructures. *Phys. Rev. B* **2011**, *84*, 174406.
(34) Lewis, E. R.; Petit, D.; Jausovec, A.-V.; O'Brien, L.; Read, D. E.; Zeng, H. T.; Cowburn, R. P. Measuring Domain Wall Fidelity Lengths Using a Chirality Filter. *Phys. Rev. Lett.* **2009**, *102*, 057209.
(35) Skoric, L.; Donnelly, C.; Abert, C.; Hierro-Rodriguez, A.; Suess, D.; Fernández-Pacheco, A. Micromagnetic Modeling of Magnetic Domain Walls in Curved Cylindrical Nanotubes and Nanowires. *Appl. Phys. Lett.* **2021**, *118*, 242403.
(36) Birch, M.; Cortés-Ortuño, D.; Litzius, K.; Wintz, S.; Schulz, F.; Weigand, M.; Štefančič, A.; Mayoh, D.; Balakrishnan, G.; Hatton, P.; Schütz, G. *Toggle-like Current-Induced Bloch Point Dynamics of 3D Skyrmion Strings in a Room-Temperature Nanowire*. 2022, Version 1; Research Square, DOI: 10.21203/rs.3.rs-1235546/v1 (accessed Jan. 10, 2022).
(37) Harinarayana, V.; Shin, Y. C. Two-Photon Lithography for Three-Dimensional Fabrication in Micro/Nanoscale Regime: A Comprehensive Review. *Opt. Laser Technol.* **2021**, *142*, 107180.
(38) Abert, C.; Exl, L.; Bruckner, F.; Drews, A.; Suess, D. Magnum.Fe: A Micromagnetic Finite-Element Simulation Code Based on FEniCS. *J. Magn. Magn. Mater.* **2013**, *345*, 29−35.

(39) Geuzaine, C.; Remacle, J.-F. Gmsh: A 3-D Finite Element Mesh Generator with Built-in Pre- and Post-Processing Facilities. *Int. J. Numer. Methods Eng.* **2009**, *79*, 1309−1331.
(40) Aballe, L.; Foerster, M.; Pellegrin, E.; Nicolas, J.; Ferrer, S. The ALBA Spectroscopic LEEM-PEEM Experimental Station: Layout and Performance. *J. Synchrotron Radiat.* **2015**, *22*, 745−752.
(41) Foerster, M.; Prat, J.; Massana, V.; Gonzalez, N.; Fontsere, A.; Molas, B.; Matilla, O.; Pellegrin, E.; Aballe, L. Custom Sample Environments at the ALBA XPEEM. *Ultramicroscopy* **2016**, *171*, 63−69.
(42) Skoric, L. *XMCDpy*, version v1.2; Zenodo, 2021, DOI: 10.5281/zenodo.5094555.
(43) Skoric, L. *XMCD* Projection, version v1.0, Zenodo, 2021, DOI: 10.5281/zenodo.5094531.

https://doi.org/10.1021/acsnano.1c10345
ACS Nano 2022, 16, 8860−8868